Silicate-mediated interstellar water formation: a theoretical study

Germán Molpeceres,[1] Albert Rimola [ID],[2]⋆ Cecilia Ceccarelli,[3] Johannes Kästner,[4] Piero Ugliengo [ID][5] and Belén Maté[1]

[1]*Instituto de Estructura de la Materia, IEM-CSIC, Serrano 123, E-28006, Madrid, Spain*
[2]*Departament de Química, Universitat Autònoma de Barcelona, E-08193 Bellaterra, Spain*
[3]*Institut de Planétologie et d'Astrophysique de Grenoble (IPAG), Univ. Grenoble Alpes, CNRS, F-38000 Grenoble, France*
[4]*Institute for Theoretical Chemistry, University of Stuttgart, Pfaffenwaldring 55, D-70569 Stuttgart, Germany*
[5]*Dipartimento di Chimica and Nanostructured Interfaces and Surfaces (NIS), Università degli Studi di Torino, Via P. Giuria 7, I-10125 Torino, Italy*

ABSTRACT

Water is one of the most abundant molecules in the form of solid ice phase in the different regions of the interstellar medium (ISM). This large abundance cannot be properly explained by using only traditional low-temperature gas-phase reactions. Thus, surface chemical reactions are believed to be major synthetic channels for the formation of interstellar water ice. Among the different proposals, hydrogenation of atomic O (i.e. $2H + O \rightarrow H_2O$) is a chemically 'simple' and plausible reaction toward water formation occurring on the surfaces of interstellar grains. Here, novel theoretical results concerning the formation of water adopting this mechanism on the crystalline (010) Mg_2SiO_4 surface (a unequivocally identified interstellar silicate) are presented. The investigated reaction aims to simulate the formation of the first water ice layer covering the silicate core of dust grains. Adsorption of the atomic O as a first step of the reaction has been computed, results indicating that a peroxo (O_2^{2-}) group is formed. The following steps involve the adsorption, diffusion, and reaction of two successive H atoms with the adsorbed O atom. Results indicate that H diffusion on the surface has barriers of 4–6 kcal mol^{-1}, while actual formation of OH and H_2O present energy barriers of 22–23 kcal mol^{-1}. Kinetic study results show that tunneling is crucial for the occurrence of the reactions and that formation of OH and H_2O are the bottlenecks of the overall process. Several astrophysical implications derived from the theoretical results are provided as concluding remarks.

Key words: astrochemistry – molecular processes – ISM: atoms – ISM: molecules.

1 INTRODUCTION

The formation of water in astrophysical environments has been, is, and will be a subject of intense research. This is because water is a molecule of fundamental relevance in the astrochemical context for several reasons.

First, it is the most abundant molecule in the Universe in the solid phase in the form of ice, (e.g. Gillett & Forrest 1973; Whittet et al. 1988; Gibb et al. 2004; Boogert et al. 2008), and among the most abundant gaseous species in regions where it is not frozen (when the dust temperature exceeds ∼ 100 K), notably in star-forming regions (e.g. Cernicharo et al. 1994, 1997; Ceccarelli, Hollenbach & Tielens 1996; Liseau et al. 1996; Doty & Neufeld 1997; Ceccarelli et al. 1999; Kristensen et al. 2012; Herpin et al. 2017). As a consequence, the chemical composition of these regions is governed by the water abundance and how little oxygen is left to form other species,

(e.g. Hollenbach et al. 2009; van Dishoeck et al. 2011; van Dishoeck, Herbst & Neufeld 2013). In addition, given its high abundance, water lines are the dominant gas coolant in hot regions, and they can be so efficient that the gas and dust could be thermally decoupled, with the gas cooler than the dust even at high ($\geq 10^7$ cm^{-3}) densities (e.g. Crimier et al. 2009; Karska et al. 2013). Furthermore, water is observed not only in the Milky Way but also in distant, high-redshift ($z \geq 2$) galaxies where it is considered a very precious proxy to measure star formation in the early Universe, (e.g. Omont et al. 2011, 2013; Liu et al. 2017). Finally, water is a crucial molecule for terrestrial life and its presence is considered a mandatory criterion for the habitability of exo-planets (e.g. Güdel et al. 2014; Silva et al. 2017), and hence, a proxy for the search of life elsewhere in the Universe.

Literature on interstellar water has been published since the early 1970s of the last century (Herbst & Klemperer 1973). The general agreement in the astrochemical community is that the formation of water occurs both in the gas phase and on the surfaces of the interstellar grain surfaces. For the gas-phase formation, two main

mechanisms are considered: low-temperature ion-neutral and high-temperature neutral–neutral synthetic routes (e.g. Hollenbach & McKee 1989; van Dishoeck et al. 2013). However, these two mechanisms are not efficient enough to explain the measured water large abundances, particularly in the form of ice. Thus, interstellar water is considered to be efficiently formed by reactions occurring on the surfaces of the interstellar grains, both on the bare refractory surfaces and on the ice mantles (Tielens & Hagen 1982).

In this paper, we present a new theoretical study on the water formation on the bare silicate surfaces. The article is organized as follows. We first briefly review the previous studies on the water surface formation (Section 2) and the novelty introduced by the present study (Section 3), then we present the adopted theoretical method (Section 4), provide the results of our new computations (Section 5), and discuss the astrophysical implications (Section 6). Conclusions are finally drawn (Section 7).

2 WATER FORMATION ON GRAIN SURFACES: PREVIOUS STUDIES

Interstellar grains are composed of two types of refractory material (Hoyle & Wickramasinghe 1969; Jones et al. 2013): carbonaceous grains, which include graphite, amorphous carbon, hydrogenated amorphous carbon, and silicon carbide (Duley 1988; Witt & Schild 1988; Amari et al. 1990; Duley 1994; Furton, Laiho & Witt 1999; Draine & Li 2007), and silicates, which can mainly be found in an amorphous state although crystalline phases have also been detected (Witt, Gordon & Furton 1998; Furton et al. 1999; Li & Draine 2001; Bowey, Rawlings & Adamson 2004; Li, Zhao & Li 2007; Henning 2010; Fogerty et al. 2016). Among the most astrophysical relevant silicates, olivines (with general formula $Mg_{2x}Fe_{(2x-2)}SiO_4$) have been thoroughly studied and positively identified by infrared spectroscopy (Henning 2010) and by identification of refractory material carried by the STARDUST mission (Zolensky et al. 2006). There is consensus that the silicate dust grains are mostly formed in the stellar outflows of dying stars, appearing to be partially crystalline and very Mg-rich, and, at a lesser extent (but this is very debated) in the supernovae (De Looze et al. 2017). The Mg-pure olivine is called forsterite (Mg_2SiO_4).

The most-studied reaction on silicate surfaces, both from theoretical and experimental point of view, is by far the formation of H_2, which is considered as the archetype reaction in gas–grain studies (Pirronello et al. 1997a,b; Katz et al. 1999; Cazaux & Tielens 2002; Goumans et al. 2009b; Vidali et al. 2009, Vidali 2013; Goumans & Bromley 2011; Downing et al. 2013; Garcia-Gil et al. 2013; Kerkeni & Bromley 2013; Navarro-Ruiz et al. 2014a, 2015, 2016; Kerkeni, Bacchus-Montabonel & Bromley 2017; Wakelam et al. 2017). The reaction of water formation on grain surfaces is also a chemical process of great interest that has been studied experimentally and theoretically. The different experiments indicate that interstellar water can be formed through a chemical network defined by different channels (e.g. Hama & Watanabe 2013), as sketched in Fig. 1.

One reactive channel is the hydrogenation of atomic O (Dulieu et al. 2010; Jing et al. 2011, 2013), in which H (or D) and O beams deposited on grain-analogues react to give H_2O following the network:

$$H + O \rightarrow OH \qquad (1)$$
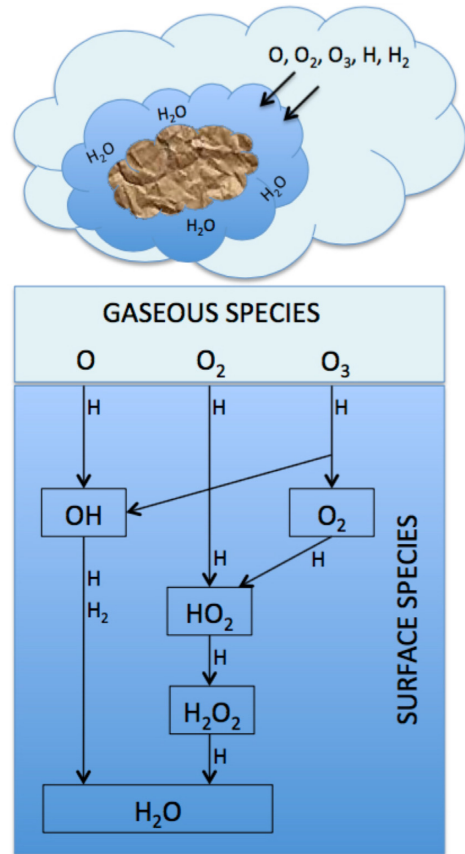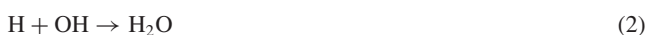
$$H + OH \rightarrow H_2O \qquad (2)$$

Figure 1. Sketch of the reaction network involved in the formation of water on the grain surfaces (adapted from Ceccarelli et al. 2014).

Another channel is the hydrogenation of molecular O_2 (Ioppolo et al. 2008, 2010; Matar et al. 2008; Miyauchi et al. 2008; Oba et al. 2009; Cuppen et al. 2010; Chaabouni et al. 2012; Accolla et al. 2013; Jing et al. 2013), in which water formation is identified by sending H (or D) atoms on O_2 ices through previous H_2O_2 formation as intermediate (Oba et al. 2014):

$$H + O_2 \rightarrow HO_2 \qquad (3)$$

$$H + HO_2 \rightarrow H_2O_2 \qquad (4)$$

$$H + H_2O_2 \rightarrow H_2O + OH \qquad (5)$$

A third path is hydrogenation of O_3 (Mokrane et al. 2009; Oba et al. 2011, 2012; Romanzin et al. 2011; Jiao & Gianfranco 2014), in which O_3 deposited or grown on a cold substrate is transformed into H_2O when reacting with H (or D) following the scheme:

$$H + O_3 \rightarrow OH + O_2 \qquad (6)$$

$$H_2 + OH \rightarrow H_2O + H \qquad (7)$$

Formation of OH as a first step is crucial (reaction 6), since the formed OH can subsequently react with atomic hydrogen through reaction (2) or with molecular hydrogen (reaction 7). Please note

that, in this last case, tunneling effects are fundamental in the final water formation.

Due to the large abundances of molecular hydrogen and atomic oxygen in the dark molecular clouds (e.g. Caux et al. 1999; Lis et al. 2001), the reaction of O with H_2 has also been proposed to contribute to the formation of water (reaction (8) and reaction (9)), as follows:

$$H_2 + O \rightarrow OH + H \qquad (8)$$

$$H_2 + O \rightarrow H_2O \qquad (9)$$
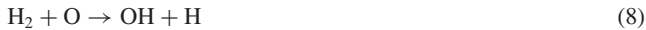
Reaction 8, leading to OH which can subsequently react with H (reaction 2), is excluded both from experiments and astrochemical models (Oba et al. 2012; Taquet et al. 2013). In contrast, for reaction 9, a combination of experimental results with kinetic Monte Carlo modelling indicates that it contributes about 11 per cent of formed water in dense interstellar clouds (Lamberts et al. 2014).

From a theoretical perspective, several works have addressed the adsorption of water on silicate surfaces by means of either classical potentials or electronic structure quantum chemical methods (de Leeuw et al. 2000, 2010; Muralidharan et al. 2008; King et al. 2010; Asaduzzaman et al. 2013; Prigiobbe, Suarez Negreira & Wilcox 2013). In contrast, theoretical studies focusing on the water formation reactions on the grain surfaces are practically missing. In that respect, the work of Goumans et al. (2009a) is of particular interest. These authors studied the hydrogenation of atomic O (i.e. reaction 1 and reaction 2) by means of QM/MM simulations using a cluster model of 34 atoms mimicking the (010) crystalline forsterite surface, in which the QM part, calculated at the MPWB1K functional with polarized double zeta basis set, was embedded in an array of point charges. They found that the steps associated with the reaction are exoergic with relatively low activation energies (6.2 and 5.2 kcal mol^{-1} for reaction 1 and reaction 2, respectively). Other theoretical works addressed the problem of the formation of water but on the surfaces of water ice (Lamberts et al. 2016; Meisner, Lamberts & Kästner 2017), not silicates.

3 PRESENT WORK OUTLINE

Improvement of the quality of gas–grain reaction databases alongside astrochemical model predictions strongly relies on the energetic values and kinetic rate constants, which could be derived from experiments. However, often experiments cannot provide reliable answers and these values are, therefore, often based on rough and, in some cases, only guessed estimates. In this context, theoretical calculations based on quantum mechanical methods are extremely useful, if not unique tools to provide reliable estimates of the above parameters. In this work, we present theoretical results on the water formation reaction routes on crystalline forsterite. To this end, we make use of periodic quantum chemical simulations on an Mg_2SiO_4 (010) crystal surface. The reactions considered are the hydrogenation of atomic O (reaction 1) and OH (reaction 2), respectively.

In general, surface reactions can adopt three possible mechanisms: i) Langmuir–Hinshelwood (Langmuir 1922; Hinshelwood 1930),which involves adsorption of the reacting species on the surface, followed by diffusion and reaction; (ii) Eley–Rideal 'prompt atom' (Eley & Rideal 1940; Eley 1941), in which a species coming from the gas phase directly reacts with species which were previously adsorbed; and (iii) Harris–Kasemo 'hot-atom' (Harris & Kasemo 1981), in which one species lands on the surface with excess of translation energy, diffuses on the surface losing partly its

translational energy, and reacting finally with the other pre-adsorbed species.

In this paper, we have considered the Langmuir–Hinshelwood (LH) mechanism as it is usually considered to be the dominant process in the ISM due to the formation of long-lasting adsorbates in the surface (e.g. Morisset et al. 2003). Thus, in addition to the actual reactions 1 and 2, we took into account both the adsorption of the reacting species and their diffusion so to obtain an overall picture of the reaction process. With our paper, we present a comprehensive quantum chemical study using a posteriori Grimme-based dispersion-corrected B3LYP-D2* Hamiltonian combined with flexible gaussian-type orbitals to theoretically characterize the H/O adsorption and H_2O formation on a slab model for the (010) crystalline forsterite (Mg_2SiO_4) surface adopting a full *ab initio* periodic approach. In practice, the silicate surface is represented by a slab model of finite thickness, thus ensuring that long-range effects are accounted for, in which all the electrons of the atoms are explicitly considered. Beyond the work of Goumans et al. (2009a), different adsorption sites, including their inter-conversion steps, and the paths leading to H_2O formation have been characterized. Additionally, estimates of tunneling effects in the reaction steps have also been considered.

The results of our new computations, therefore, provide a comprehensive atomic-scale insight on the formation of interstellar water on silicate surfaces, which can be viewed as the initial step of the formation of water ices on bare grains (namely, proto-ice mantles). In practice, our computations describe the water ice formation process in the environments present at the edge of molecular clouds, where FUV photons keep the oxygen prevalently in the gaseous atomic form. Finally, we expect the energetic data and rate constant provided in this paper to be useful in astrochemical modelling studies, improving their theoretical predictions.

4 METHODS

4.1 Surface model

In this paper, a non-polar periodic slab model mimicking the crystalline (010) forsterite surface has been used, as proposed by Navarro-Ruiz et al. (2014b). The surface model was obtained by cutting out from the bulk system a slab parallel to the (010) crystalline plane. Compared to the primitive unit cell, the c lattice parameter was enlarged twice to avoid mutual interactions between adsorbed species of adjacent cells. The final structure of the bare surface contains 56 atoms (see Figs. 2(A) and (B)). The optimized lattice parameters of the bare surface model are a = 4.7892 Å and c = 12.0183 Å, and a thickness of about 10.2 Å, close to the original bulk unit cell b value (10.254 Å). The outermost atoms exposed to the external surface of our slab model are tricoordinated Mg^{2+} cations (which are undercoordinated compared to Mg^{2+} bulk atoms) and O atoms. Calculated electrostatic potential maps show positive and negative potential regions around the Mg and O atoms, respectively. This surface slab model has been validated (Navarro-Ruiz et al. 2014b) and used over the past years for the formation of H_2 (Navarro-Ruiz et al. 2014a, 2016), and very recently to study the adsorption of organic molecules present in meteorites (Rimola, Trigo-Rodriguez & Martins 2017).

4.2 Computational methods

All the calculations in this paper have been done using Gaussian09 (Frisch et al. 2009) for minimal cluster calculations and CRYS-
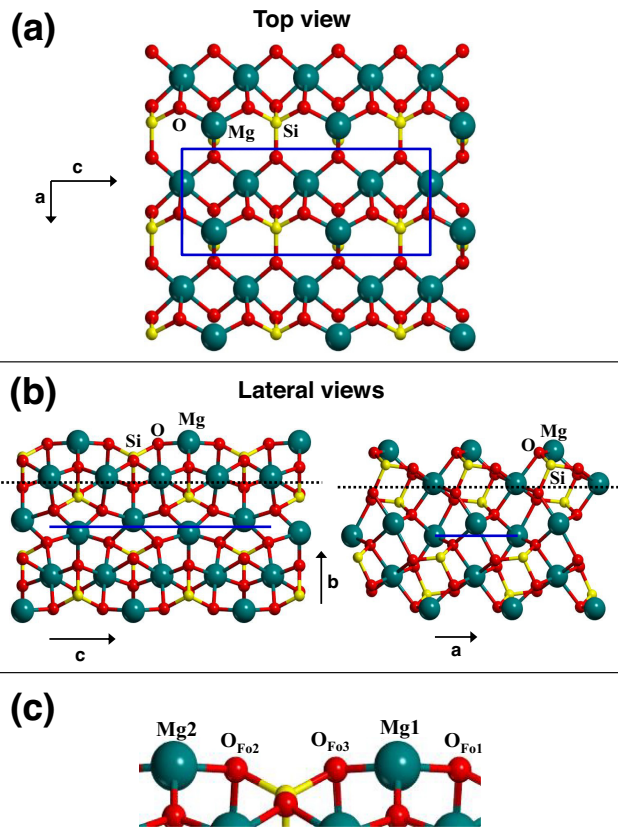
Figure 2. Top (a) and lateral (b) views of the non-polar crystalline (010) forsterite Mg_2SiO_4 surface model used in this work (see text for details). The unit cell is highlighted in blue. Atoms above the dashed lines are those included in the frequency calculations. c) Labels used in this work for the most important atoms belonging to the surface; namely, for magnesium cations, Mg1 and Mg2; for surface oxygen atoms, O_{Fo1}, O_{Fo2} and O_{Fo3}.

TAL14 (Dovesi et al. 2014) for the periodic calculations. Minimal cluster calculations have been carried out to perform a preliminary calibration study to identify a suitable density functional method with which to perform the periodic calculations. This calibration study was focused on the adsorption of atomic O on the outermost Mg atoms. The fundamental electronic state of O is ^{3}P. However, its adsorption on the forsterite surface can lead to electronic structure reorganizations, resulting in either a singlet or triplet spin configuration. Therefore, the aim of the calibration study is to compare the energy difference between the triplet and singlet states calculated with different DFT methods and at the coupled cluster CCSD(T) level on a minimal cluster model consisting of the first Mg coordination sphere. Results of the calibration study and the cluster model adopted are available as on-line material in Appendix.

The results of this calibration study indicate that the singlet state is more favorable by 29.7 kcal mol^{-1} than the triplet one. Moreover, we have found that the hybrid B3LYP (Becke 1993; Lee, Yang & Parr 1988) functional gives fairly comparable results with the CCSD(T) ones. It is worth mentioning that other functionals give closer results to the CCSD(T) ones. However, they are not implemented in CRYSTAL14, and hence our final choice to use B3LYP for periodic calculations. For these periodic calculations, moreover, the a posteriori D2* correction to account for dispersion was also used, in which the initial parametrization proposed by Grimme (Grimme 2006) (D2) was modified to be used for periodic

systems using this functional (Civalleri et al. 2008; Civalleri et al. 2010; Rimola, Civalleri & Ugliengo 2010a). Transition state (TS) search has been performed using the distinguished reaction coordinate (DRC) technique as implemented in CRYSTAL14 (Rimola et al. 2010b). Nature of the stationary points has been checked, in which for transition state structures one, and only one, imaginary frequency was obtained by Hessian matrix diagonalization, while for minima all frequencies were real. For all calculations involving open-shell systems, the unrestricted formalism was used. Mulliken population analysis has been performed to evaluate the charges and electron spin densities on the atoms.

Both CRYSTAL14 and Gaussian09 use Gaussian-Type Orbitals (GTOs) as basis sets to represent the electronic wave function. For periodic geometry optimizations, the following all-electron contractions have been used (hereafter referred to as B1): (8s)-(831sp)-(1d) for Si, (6s)-(31sp)-(1d) for O, (6s)-(631sp)-(1d) for the top-layer Mg atoms (standard 6-31G(d,p) Pople basis set), and (8s)-(511sp)-(1d) for the remaining, internal Mg atoms. To improve the accuracy of the energetics of the processes to study, single-point energy calculations onto the optimized geometries have been done using the following larger contractions (hereafter referred to as B2): (8s)-(831sp)-(1d) for Si; (6s)-(311sp)-(1d) for O; (631111s)-(42111p)-(1d) for the top-layer Mg atoms (standard 6-311G(d,p) Pople basis set); and (8s)-(511sp)-(1d) for the remaining Mg atoms. For all calculations, a TZP basis set from Ahlrichs and coworkers (Schafer, Horn & Ahlrichs 1992), i.e. (311s)-(1p), has been used for the H atoms. For the cluster-based benchmark calculations, CCSD(T) calculations were combined with the Dunning's aug-cc-pVTZ basis set (Woon & Dunning 1994), while for the DFT methods with a 6-31G(d,p) basis set, since this is the most comparable basis set for CRYSTAL14 optimizations.

The shrinking factor of the reciprocal space net (Monkhorst & Pack 1976), defining the mesh of k points in the irreducible Brillouin zone, was set to 3, which requires the diagonalization of the Hamiltonian matrix in 5 k points. The overlap integrals controlling the Coulomb and exchange series were set to 10^{-6} and 10^{-16}. The grid for the Gauss–Legendre and Lebedev quadrature schemes was set to the default values, namely (75, 974), in the evaluation of functionals. The SCF convergence was set to 10^{-7} Hartree.

Geometry optimizations were carried out by keeping fixed the cell parameters at the optimized bare surface values so that only the internal atomic positions were optimized via analytic energy gradients (Doll 2001). The geometry optimization was performed by means of a quasi-Newton algorithm in which the quadratic step (BFGS Hessian updating scheme) is combined with a linear one (Civalleri et al. 2001).

The adsorption energies ΔE of the species; namely, O and H atoms, per unit cell were calculated as:

$$\Delta E = E(SM//SM) - E(S//S) - E_m(M) \qquad (10)$$

where $E(SM//SM)$ is the absolute energy per unit cell of the optimized adduct involving the species adsorbed on the surface, $E(S//S)$ is the absolute energy per unit cell of the optimized bare forsterite surface, and $E_m(M)$ is the absolute energy per unit cell of the isolated species. The use of finite GTOs basis sets is implicitly associated with a basis set superposition error (BSSE). Calculations using the B1 basis set, BSSE is significant; nevertheless, it has been proven that for B2 calculations the amount of BSSE is dramatically reduced (Navarro-Ruiz et al. 2014a). Therefore, for the sake of clarity, values presented along the work are those calculated at B2 level including zero-point energy corrections (see below) at the B1 level.

Zero-point energy (ZPE) and thermal corrections to the adsorption energies were calculated using standard statistical thermodynamics formulae within the harmonic approximation. By diagonalizing the mass-weighted matrix, the vibrational frequencies were calculated at the Γ point. This was achieved by numerical differentiation of the 1st-energy derivatives, i.e. each equilibrium nuclear coordinates were displaced by 0.003 Å (Pascale et al. 2004). However, to save computational time, this was only done taking only a fragment of the system into account (Fig. 2B shows the atoms considered).

Since the processes under study are considered to occur at very low temperatures, alongside that H atoms are implicated, tunneling effects were accounted for. The tunneling crossover temperature (T_X), which indicates that below of which tunneling is important, was first calculated adopting the formula by Fermann and Auerbach (Fermann & Auerbach 2000):

$$T_X = \frac{h\nu^{\neq} \Delta U_0^{\neq}/k_B}{2\pi \Delta U_0^{\neq} - h\nu^{\neq} ln2}, \quad (11)$$

where $\nu^{\neq}$ is the frequency of the transition normal mode, h is the Planck constant, $\Delta U_0^{\neq}$ is the ZPE-corrected energy barrier, and k_B is the Boltzmann constant. Moreover, we calculated rate constants in a semiclassical way (k^{SC-FA}), in which tunneling contributions are accounted for by introducing the transmission coefficient $\kappa^{FA}(T)$ developed by Fermann & Auerbach (2000) into the classical rate constant (k^{TST}), which is calculated with the Eyring's conventional transition state theory, i.e.:

$$k^{SC-FA}(T) = k^{TST} \times \kappa^{FA}(T) \quad (12)$$

$$\kappa^{FA}(T) = exp\left(\frac{\Delta U_0^{\neq}}{k_B T}\right) exp\left(-\frac{2\pi \Delta U_0^{\neq}}{h\nu^{\neq}}\right)\left(1 + \frac{2\pi k_B T}{h\nu^{\neq}}\right) \quad (13)$$

$$k^{TST} = \frac{k_B T}{h} exp\left(-\frac{\Delta G^{\neq}}{RT}\right), \quad (14)$$

where $\Delta G^{\neq}$ is the free energy barrier calculated at the temperature T.

Additionally, we calculated the tunneling contribution by the Eckart approximation, which is a 1D tunneling correction, i.e. it takes tunneling into account along the reaction coordinate only. The Eckart-corrected rate constant ($k^{SC-Eckart}$) is obtained as

$$k^{SC-Eckart}(T) = k^{TST} \times \kappa^{Eckart}(T) \quad (15)$$

where $\kappa^{Eckart}(T)$ is calculated as the fraction of classical and quantum flux through a one-dimensional barrier:

$$\kappa^{Eckart}(T) = \frac{1}{k_B T} exp\left(-\frac{\Delta G^{\neq}}{RT}\right) \int_0^{\infty} P(E) exp\left(-\frac{E}{RT}\right) dE \quad (16)$$

The transmission probability is calculated analytically (Eckart 1930) for an Eckart barrier with the same $\Delta U_0^{\neq}$ and $\nu^{\neq}$ as the reactions under study.

5 RESULTS

This section is organized as follows. First, results devoted to the adsorption of atomic O on the (010) forsterite surface are presented (Section 5.1). In this part, different electronic states of the atomic O adsorbed on the surface are analyzed. Then, the potential energy surfaces for the hydrogenation of the O-adsorbed atom leading to water formation are shown, putting special emphasis on structure and energy-related features of the adsorption, diffusion, and reaction of the H atoms (Section 5.2 and 5.3). Finally, kinetic analyses, including tunneling effects, associated with the simulated processes are presented (Section 5.4).

For the sake of clarity, the outermost atoms of the (010) Mg_2SiO_4 surface model involved in the adsorption and reactivity will be referred to using the labels shown in Fig. 2(C); that is, for the Mg cations as Mg1 and Mg2, and for the surface O atoms as O_{Fo1}, O_{Fo2}, and O_{Fo3}. Table 1 summarizes the calculated energetic values for the different processes considered in this work in different units, namely kcal mol^{-1}, eV, and K.

5.1 Adsorption of O atoms

The ground electronic state of atomic O is ^3P, since it has two unpaired electrons with spins of the same sign lying on degenerated atomic orbitals. However, interaction with the surface can induce electronic structure reorganizations, so that O adsorption can result in either a singlet or triplet spin configuration. These two possible electronic states have been calculated at a periodic level. The optimized geometries are shown in Fig. 3(A). The spin densities for these systems are reported as supplementary on-line material.

In the singlet state, adsorption on both Mg1 and O_{Fo1} has been attempted, but in both cases the optimized geometry collapses onto the same geometry (Fo-O^S of Fig. 3A), Here, a peroxo O_2^{2-} group is formed on the surface. That is, the O atom (hereafter referred to as O_{atom}) attaches on the Mg1 cation but also binds on the O_{Fo1} atom, thus forming a peroxo complex. The O_{atom}–Mg1–O_{Fo1} angle is of 44 degrees and the O_{atom}–O_{Fo1} bond length 1.529 Å. The Mulliken charges of O_{atom} and O_{Fo1} are −0.48 e and −0.80 e, respectively, revealing that a charge transfer from O_{Fo1} to O_{atom} takes place, thus binding them as a peroxo ion. The spin density on O_{atom} is 0.0, indicating that the unpaired electrons of the isolated O(^3P) atom couple to yield the singlet state. This coupling is caused by the loss of the degeneracy of the atomic orbitals as a consequence of the surface interaction. Formation of a surface peroxo complex due to O adsorption has already been described, particularly on regular alkaline–earth oxides (i.e. MgO, CaO, SrO, and BaO), Cu_2O, and α-alumina surfaces (Kantorovich & Gillan 1997; Geneste, Morillo & Finocchi 2005; Di Valentin et al. 2006; Gamallo & Sayos 2007; Pasti, Baljozovic & Skorodumova 2015; Yu et al. 2015).

The analogue system in the triplet electronic state was calculated using as initial guess structure Fo-O^S, resulting with the Fo-O^T structure (see Fig. 3A). Here, the peroxo complex is broken (O_{atom}–O_{Fo1} bond distance of 2.230 Å), the O_{atom} remaining exclusively adsorbed on the surface Mg1 cation. In Fo-O^T, the spin densities on O_{atom} and O_{Fo1} are +1.68 and + 0.32, respectively, so that accordingly to Pauli repulsion, the peroxo group becomes broken.

At variance with the gas-phase O atom, on the (010) Mg_2SiO_4 surface model, the singlet state is more stable than the triplet one, the calculated adsorption energies being −31.9 and −1.7 kcal mol^{-1} for Fo-O^S and Fo-O^T, respectively. This is in agreement with the O adsorptive features on the above-mentioned oxide surfaces (Kantorovich & Gillan 1997; Geneste et al. 2005; Di Valentin et al. 2006; Gamallo & Sayos 2007; Pasti et al. 2015; Yu et al. 2015), although the calculated adsorption energies on these oxides are more favourable (between −44 and −53 kcal mol^{-1}). The larger adsorption energy given by Fo-O^S compared to Fo-O^T is due to the formation of the peroxo group, which is associated with a chemisorption process, while O adsorption in Fo-O^T can be understood as a physisorption process. Note that the energy difference between Fo-O^S and Fo-O^T, 30.2 kcal mol^{-1}, is very similar to that calculated at

Table 1. Potential reaction energies (ΔE) and including zero-point energy corrections (ΔU^0) for the different processes considered in this work, with different energy units.

Reaction	ΔE			ΔU^0		
	kcal mol^{-1}	eV	K	kcal mol^{-1}	eV	K
$O(^3P) + Fo \rightarrow Fo\text{-}O^S$	-33.6	-1.45	-16895	-31.9	-1.39	-16089
$O(^3P) + Fo \rightarrow Fo\text{-}O^T$	-3.2	-0.14	-1630	-1.7	-0.08	-898
$Fo\text{-}O^S + H \rightarrow D1$	-6.0	-0.26	-3018	-4.3	-0.18	-2170
$Fo\text{-}O^S + H \rightarrow D2$	-74.3	-3.22	-37384	-68.2	-2.96	-34311
$Fo\text{-}OH \rightarrow Fo + OH$	$+30.0$	$+1.30$	$+15086$	$+27.6$	$+1.19$	$+13877$
$Fo\text{-}OH + H \rightarrow D3$	-6.4	-0.27	-3205	-4.6	-0.20	-2331
$Fo\text{-}OH + H \rightarrow D4$	-90.2	-3.91	-45367	-83.5	-3.62	-42012
$Fo\text{-}H_2O \rightarrow Fo + H_2O$	$+27.1$	$+1.17$	$+13631$	$+24.4$	$+1.05$	$+12261$
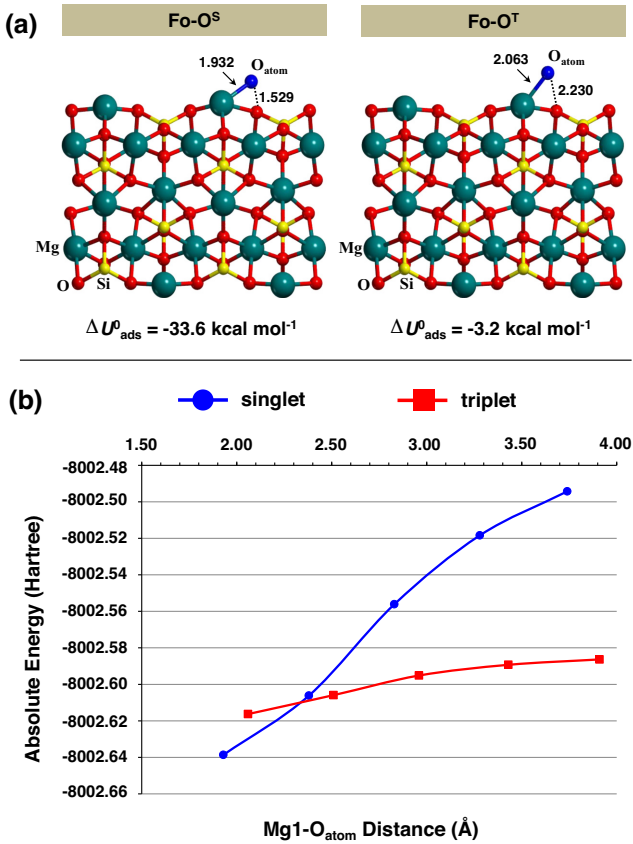
Figure 3. (a) B3LYP-D2*-optimized geometries for the adsorption of atomic oxygen (O_{atom}, in blue) on the (010) forsterite Mg_2SiO_4 surface model, in the singlet (Fo-O^S) and triplet (Fo-O^T) electronic states. O_{Fo} (in red) refers to the oxygen atoms belonging to forsterite surface. Calculated $O(^3P)$ adsorption energies (including ZPE corrections) with respect to the bare (010) forsterite surface are also included (ΔU^0_{ads} values). Bond distances are in Å. (b) DRC of the $Mg1$–O_{atom} distance in the singlet (blue) and triplet (red) electronic states.

CCSD(T) using the minimal cluster, 29.7 kcal mol^{-1}, thus indicating a very good accuracy of the method employed.

The O adsorption energy calculated in Goumans et al. (2009a) is about -103 kcal mol^{-1}, by far more favourable than the one calculated here. While these differences may well be due to the different computational approaches, it is important to remark that in their work the O adsorption takes place when the first H atom is already on the surface, in particular on an O atom analogue to our O_{Fo3}. This can have important implications in the calculated

values since different electronic reorganizations take place during the O adsorption. Indeed, while in our case the adsorption leads to the formation of the peroxo group, in the Goumans' work, the H-containing silicate surface has the spin density arising from the H atom on the Mg cation. Due to that, the O adsorption occurs on this Mg cation (no peroxo group is formed), as it is driven by a very favorable spin–spin coupling.

As the singlet state is more stable than the triplet one, it is reasonable to think that during the adsorption an inter-system crossing process can take place from the triplet to the singlet electronic states. To check this point, we have performed DRC calculations by decreasing the $Mg1$–O_{atom} distance to simulate the approach of O_{atom} to the surface calculated in both electronic states. Results are shown in Fig. 3(B), indicating that an inter-system crossing takes place at an $Mg1$–O_{atom} distance of about 2.3 Å. Probabilities for the occurrence of spin crossings are high for processes involving heavy atoms such as metals of the third row and below. However, for those involving O is low, although the Mg cation is also implicated. Thus, in our case, it is likely that the adsorption process takes place with O_{atom} in its triplet state, but once adsorbed on the surface the system relaxes to the singlet state trough any physical way such as thermal energy redistribution with the lattice phonons or, in case the grain has an enough small size, via radiative emission. It is important to stress out that subsequent diffusion processes studied in the present work are much slower than the spin relaxation mechanisms operating in this electronic state conversion.

5.2 Formation of the OH radical

Once the O atom is adsorbed, the next step towards formation of OH through reaction (1) on the Mg_2SiO_4 surface model adopting an LH mechanism is the adsorption of one H atom. All the considered structures of this section have been calculated in a doublet electronic state due to the unpaired electron of the adsorbing H atom. Fig. 4(A) shows the optimized geometries for the H adsorption on the surface model. As adsorption sites, the available Mg2 cation and its nearby O_{Fo2} atom have been identified (D1 and D2 adducts of Fig. 4A, respectively). D1 has an adsorption energy with respect to Fo-O^S of -4.3 kcal mol^{-1}. The relatively large Mg2–H bond distance (2.039 Å) and the fact that most of the spin density is on the adsorbed H atom (0.75) indicates that this structure represents a physisorption state. In contrast, D2 is a chemisorption state, in which a covalent bond between the H atom and the O_{Fo2} atom is established, with a bond distance of 0.976 Å, thus forming a surface SiOH group. The calculated adsorption energy with respect to Fo-O^S is -68.2 kcal mol^{-1}. It is worth mentioning that, although D2 is more stable than D1, according to published results for the H adsorption on the same
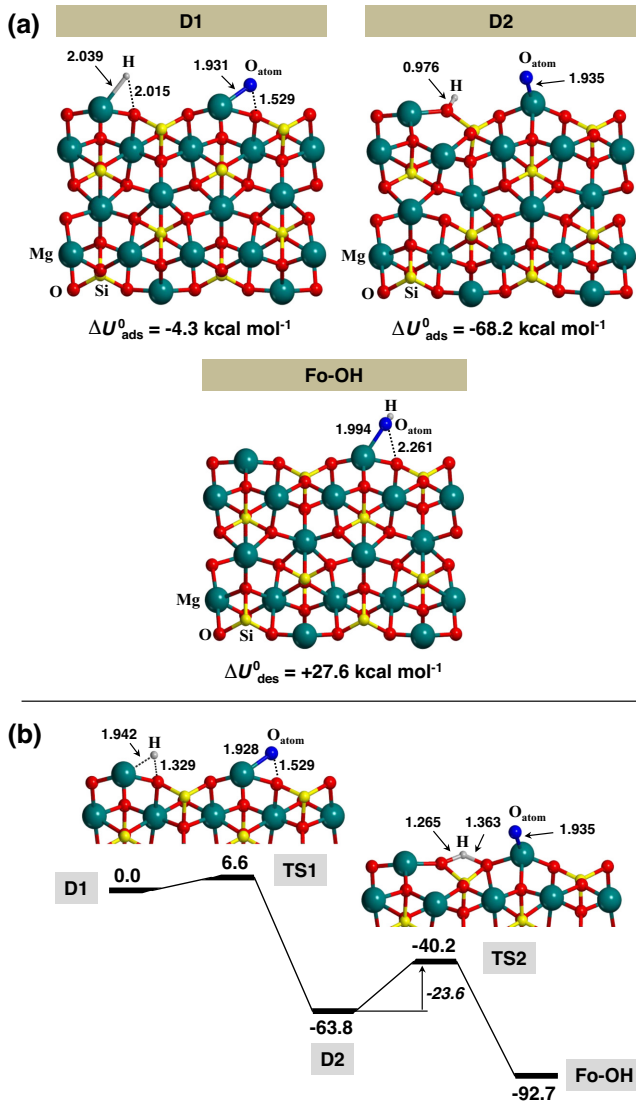
Figure 4. a) B3LYP-D2*-optimized geometries for the H adsorption in different sites of the Fo–O^S system (D1 and D2) and the complex formed when the H atom couples to the adsorbed O atom yielding OH (Fo-OH). For D1 and D2, the calculated adsorption energies including ZPE corrections of the H atom (ΔU^0_{ads}) are shown; for Fo-OH the desorption energy including ZPE corrections of the OH radical (ΔU^0_{des}) is shown. b) B3LYP-D2*-ZPE-corrected energy profile for the formation of the OH radical on the (010) Mg$_2$SiO$_4$ surface model adopting the D1 → D2 → Fo-OH path. Bond distances are in Å.

(010) Mg$_2$SiO$_4$ surface investigating the H$_2$ formation (Goumans et al. 2009b; Navarro-Ruiz et al. 2014a), formation of D2 by direct adsorption of an H atom from the gas phase has a non-negligible energy barrier, while formation of D1 is actually barrierless.

A spin density analysis (reported as on-line material) allows us to understand the structural properties of the D1 and D2 complexes. In D1, the H atom is physisorbed on the Mg2 cation, but it is tilted by 30 degrees with respect to the surface normal, being bent towards the adjacent O$_{Fo2}$ atom. The spin density on the H atom is 0.75, while most of the remaining spin density (≈ 0.20) is concentrated on O$_{Fo2}$. This spin distribution indicates that between the H and O$_{Fo2}$ atoms a hemi-bonded interaction is established, with an H–O$_{Fo2}$ bond distance of 2.015 Å and a H–Mg2–O$_{Fo2}$ angle of 61

degrees. Interestingly, the surface peroxo group remains intact upon H adsorption in D1. For D2, in contrast, the spin density is on the adsorbed O$_{atom}$ (1.00) meaning that the electron of the H atom has jumped to O$_{atom}$, thus being an 'O$^-$' anion. Because of that, the surface peroxo group is broken, and hence that the O$_{atom}$ is essentially adsorbed on the Mg1 cation.

H adsorption on the O$_{Fo3}$ atom has been attempted. However, upon optimization, the H atom couples to the adsorbed O$_{atom}$ forming an OH group on the Mg1 cation (Fo–OH adduct shown in Fig. 4A). It is worth mentioning that this H jump does not take place with the O$_{atom}$ of the same unit cell but that belonging to the adjacent cell since the orientation of the involved atoms makes this jump more feasible (see supplementary on-line material). The formed OH group is tilted by about 20 degrees with respect to the surface normal. A spin density analysis of the Fo–OH structure indicates that the spin density is 0.68 on O$_{atom}$ and 0.32 on O$_{Fo1}$ (see supplementary on-line material). Accordingly, a hemi-bonded interaction between these two oxygen atoms is established (with a O$_{atom}$–O$_{Fo1}$ distance of 2.261 Å and a O$_{atom}$–Mg1–O$_{Fo1}$ angle of 69.8 degrees), and hence that the formed OH group is bent towards the O$_{Fo1}$ atom.

Fig. 4(B) shows the ZPE-corrected energy profile for the formation of OH on the Mg$_2$SiO$_4$ surface model adopting the D1 → D2 → Fo-OH path. It is worth mentioning that the reaction path begins with D1 and not D2 since, as mentioned above, formation of D1 is barrierless, at variance with formation of D2. The first step involves the H jump from D1 to D2 and has an energy barrier of 6.6 kcal mol^{-1} (TS1 of Fig. 4B). The second step implies the H jump from O$_{Fo2}$ to O$_{Fo3}$. As mentioned above, once the H atom is on O$_{Fo3}$, the system spontaneously evolves to form the OH group. The calculated energy barrier for this second step is 23.6 kcal mol^{-1}. This value is significantly higher than that calculated for the first step, and accordingly this second step can be understood as the kinetic bottleneck of the path. Both steps involving the formation of OH are exergic so that the overall reaction energy is favourable by 92.7 kcal mol^{-1}. The work of Goumans et al.(2009a) showed an energy barrier for the OH formation of 6 kcal mol^{-1}, significantly lower than that computed by us. As mentioned in the previous section, Goumans et al. identified an activated complex with the atomic O and the H atom on the Mg1- and O$_{Fo3}$-analogue atoms, respectively. Their energy barrier was calculated as the jump of the H atom to the O adatom. This is at variance with our calculated process, in which the H atom jumps from O$_{Fo2}$ to O$_{Fo3}$, which subsequently spontaneously evolves to couple to the O$_{atom}$. The differences on the stability of the adduct in which the H atom attaches on the O$_{Fo3}$ may due to the different computational approaches between the two studies.

Desorption energy of the OH was computed to be 27.6 kcal mol^{-1}. We have simulated the desorption process by increasing the Mg1–O$_{atom}$ distance with a set of DRC calculations (shown in the supplementary on-line material). Results show a continuous increase of energy up to a plateau converging to the OH desorption energy value. This clearly indicates that there is no energy barrier in the desorption process.

5.3 Formation of the water molecule

Final formation of the H$_2$O molecule adopting reaction (2) on the Mg$_2$SiO$_4$ surface model through a LH mechanism has been computed considering the adsorption and diffusion of a second H atom. All the considered structures of this section have been calculated as a singlet electronic state but adopting an unrestricted open-shell
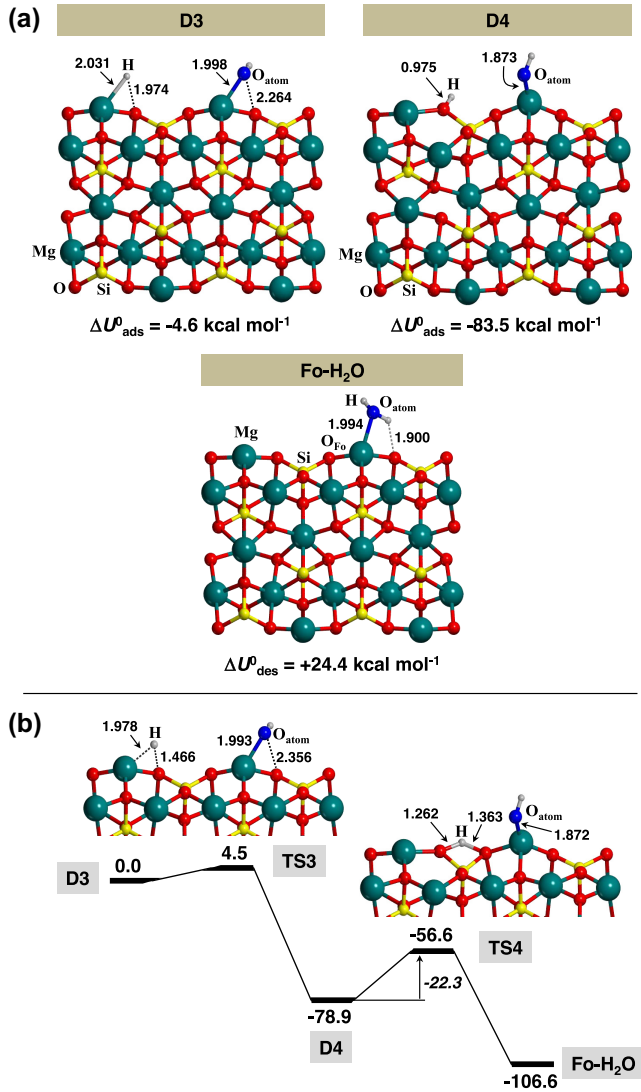
(a)

$\Delta U^0_{ads} = -4.6$ kcal mol^{-1} $\Delta U^0_{ads} = -83.5$ kcal mol^{-1}

$\Delta U^0_{des} = +24.4$ kcal mol^{-1}

(b)

Figure 5. a) B3LYP-D2*-optimized geometries for the H adsorption in different sites of the Fo–OH system (D3 and D4) and the complex formed when the H atom couples to the adsorbed O atom yielding H$_2$O (Fo-H$_2$O). For D3 and D4, the calculated adsorption energies including ZPE corrections of the H atom (ΔU^0_{ads}) are shown; for Fo-H$_2$O the desorption energy including ZPE corrections of the H$_2$O molecule (ΔU^0_{des}) is shown. b) B3LYP-D2*-ZPE-corrected energy profile for the formation of the H$_2$O molecule on the (010) Mg$_2$SiO$_4$ surface model adopting the D3 $\rightarrow$ D4 $\rightarrow$ Fo-H$_2$O path. Bond distances are in Å.

formalism. Similarly to the adsorption of the first H atom, two possible adducts have been identified for the adsorption of the second H atom (shown in Fig. 5A): (i) adsorption on the Mg2 cation (D3 adduct), and (ii) adsorption on the O$_{Fo2}$ atom (D4 adduct). Moreover, geometry optimization when the H atom is adsorbed on O$_{Fo3}$ leads to a spontaneous formation of H$_2$O (Fo-H$_2$O adduct) due to a direct coupling of the H atom with the OH group (see supplementary on-line material). D3 is a physisorbed state while D4 is a chemisorbed state, with adsorption energies of -4.6 kcal mol^{-1} and -83.5 kcal mol^{-1} with respect to Fo-OH, respectively. Similarly to D1, in D3 the spin density on the second H atom is 0.74 while on the O$_{Fo2}$ is 0.19 (see supplementary on-line material), thus establishing a hemi-bonded interaction with a H-O$_{Fo2}$ bond distance of 1.974 Å and the H-Mg2-O$_{Fo2}$ angle of 60.1 degrees. The

Table 2. B3LYP-D2* ZPE-corrected energy barriers ($\Delta U^{\neq}_0$, in kcal mol^{-1}), transition frequencies ($\nu^{\neq}$, in cm^{-1}), and tunneling crossover temperatures (T_X, in K).

Reaction	$\Delta U^{\neq}_0$	$\nu^{\neq}$	T_X
D1 $\rightarrow$ D2	6.6	1029	248
D2 $\rightarrow$ Fo-OH	23.6	1605	375
D3 $\rightarrow$ D4	4.5	1485	380
D4 $\rightarrow$ Fo-H$_2$O	22.3	1583	370

spin density on O$_{atom}$ and O$_{Fo1}$ is practically the same as in Fo-OH (0.69 and 0.31, respectively), so that the hemi-bonded interaction between these two atoms is kept. In D4, the spin density on all the involved atoms in the adsorption processes is practically 0. This means that both the unpaired electron of the second H atom and the spin density of 0.32 on O$_{Fo1}$ in Fo-OH are collected by the O$_{atom}$, which is converted formally into an 'O^{2-}' anion. Due to this spin density reorganization, the hemi-bonded interaction between O$_{atom}$ and O$_{Fo1}$ in Fo-OH is lost, and the O$_{atom}$ is exclusively attached to the Mg1 cation in the form of a hydroxide group.

Fig. 5(B) shows the ZPE-corrected energy profile for the formation of H$_2$O adopting the D3 $\rightarrow$ D4 $\rightarrow$ Fo-H$_2$O path. The first step is essentially the H jump from D3 to D4, which presents an energy barrier of 4.6 kcal mol^{-1} (TS3 of Fig. 5B). The second step is the jump of the H atom from O$_{Fo2}$ to O$_{Fo3}$ (TS4 of Fig. 5B), which as mentioned above, its optimization leads to the formation of H$_2$O. This energy barrier has been computed to be 22.4 kcal mol^{-1}, thus this second step being the bottleneck of the path. The both steps involving the H$_2$O formation are exoergic so that the overall reaction energy is favourable by -106.6 kcal mol^{-1}.

The desorption energy of the H$_2$O molecule was computed to be 24.3 kcal mol^{-1}, which is very similar to the calculated value of 22.7 kcal mol^{-1} by Goumans et al. (2009a). We have simulated the H$_2$O desorption process by performing a set of DRC calculations in which the Mg1-O$_{atom}$ distance is increased. Results (shown as supplementary on-line material) indicate a continuous increase of energy up to a plateau converging to the H$_2$O desorption energy value. This energy curve demonstrates that there is no energy barrier in the desorption process.

5.4 Kinetic study

We have performed a kinetic study for the processes described in Fig. 4(B) and Fig. 5(B); that is, those involving the H hoping on the surface and formation of OH and H$_2$O. In order to evaluate the kinetic trends of these processes, we have employed the formulations proposed by Fermann & Auerbach (FA) and by Eckart, respectively, both described in the computational methods section (Section 4). We calculated the rate constants k$^{SC–FA}$ and k$^{SC–Eckart}$ adopting the semiclassical approach by applying the transmission coefficients κ^{FA}(T) and κ^{Eckart}(T) into the conventional rate constant (k^{TST}) using the energy barriers ($\Delta U^{\neq}_0$) and the transition frequencies ($\nu^{\neq}$) obtained with the quantum chemical calculations (reported in Table 2). For the FA approach, we calculated the crossover temperature (T_X), in which above T_X we considered κ^{FA}(T) $= 1$ (and hence the abrupt change of slope below T_X).

The kinetic analysis has been performed for the four barriers under consideration. The Arrhenius plots associated with these processes are shown in Fig. 6. The first aspect to mention is the different calculated rate constant values provided by the FA and Eckart approaches. That is, $k^{SC–Eckart}$ values are systematically lower than
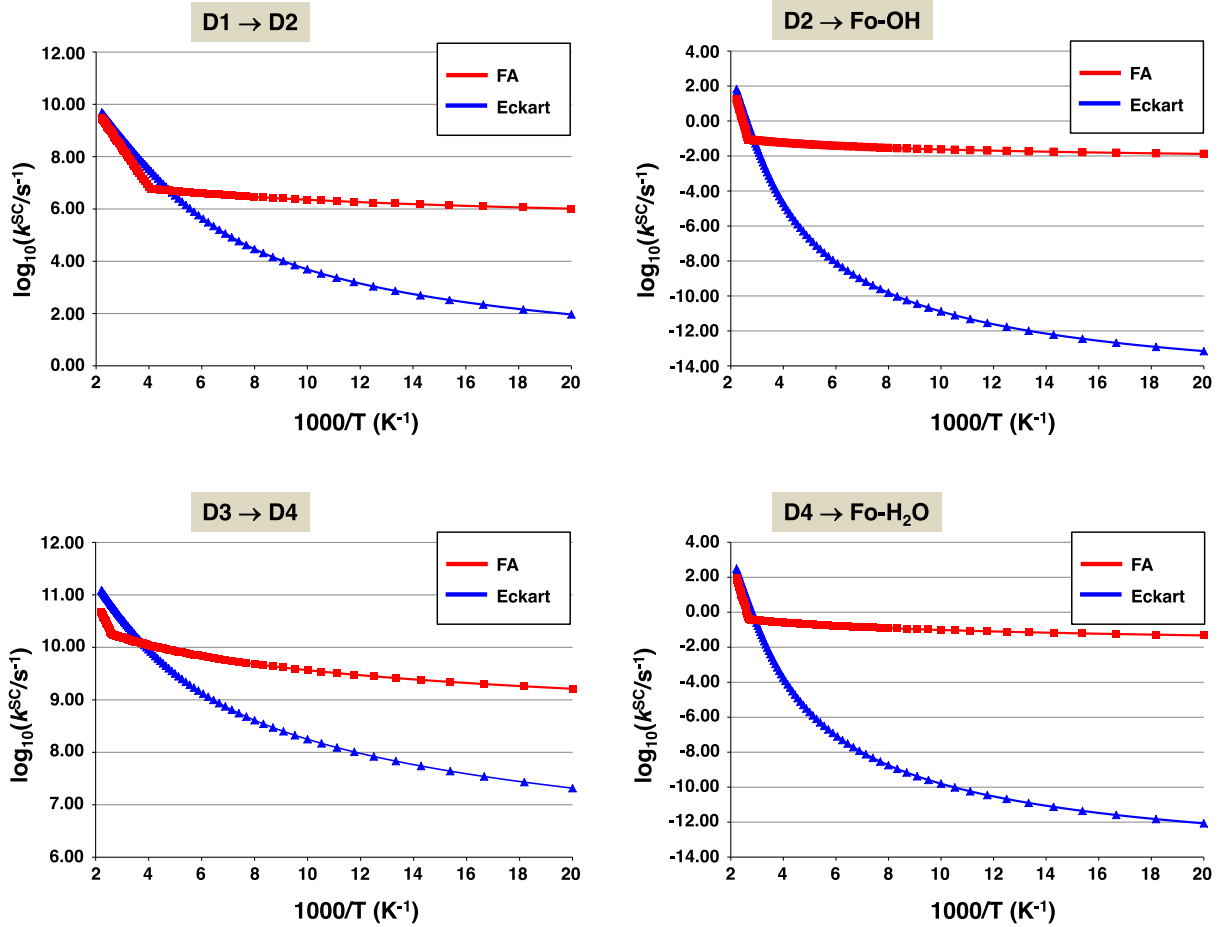
Figure 6. Arrhenius plots of $\log_{10}(k^{SC})$ between 450 and 50 K for all the processes studied in this work adopting a semiclassical approach using the Fermann & Auerbach (FA, red) and Eckart (blue) models, described in Section 4.

the k^{SC-FA} ones. In a previous work by some of us (Lamberts et al. 2016), it was detected that Eckart-based rate constants are somewhat underestimated than those computed with more rigorous approaches to compute tunneling rates (i.e. instanton theory). On the other hand, the FA approach has only been validated to temperatures as low as 150 K, so that they are probably overestimated by some amount. Therefore, the actual rate constant values may probably lay between the two approaches.

Irrespective of the kinetic approach used, according to the Arrhenius plots two different kinetic trends can be distinguished: i) conversion of a physisorbed H adatom into a chemisorbed one (i.e. D1 → D2 and D3 → D4 processes), and ii) formation of OH and H_2O as products of reactions 1 and 2 (i.e. D2 → Fo-OH and D4 → Fo-H2O). There is clear evidence that tunneling is of great importance in all processes. In all of them, there is a noticeable slope change, thus indicating that tunneling effects are present in the reactions at low temperatures. This is probably due to the high transition frequencies associated with the reactions, as all of them are above 1000 cm^{-1}. Another interesting aspect is that, in the tunneling regime, the H hopping converting the physisorption states into chemisorption ones (D1 → D2 and D3 → D4) is faster than formation of OH and H_2O. In fact, for the former processes estimated values are $k^{SC-FA} \approx 6/k^{SC-Eckart} \approx 2$ and $k^{SC-FA} \approx 9/k^{SC-Eckart} \approx 7$, respectively, while for the latter ones $k^{SC-FA} \approx -2 / k^{SC-Eckart} \approx -13$ and $k^{SC-FA} \approx -1 / k^{SC-Eckart} \approx -12$, respectively. This is due to the large differences in the energy barriers, in which in the former

cases they are significantly lower than the latter cases. According to these values, thus, formation of the OH and H_2O species can be considered as the bottlenecks of the overall process, even when tunneling effects are operating.

6 ASTROPHYSICAL IMPLICATIONS

Results shown in this work provide an atomic-scale picture, including quantitative energetic data, of the formation of a water molecule on a silicate surface. This process represents the very first step of the nucleation and growth of the water ice covering the silicate core of dust grains; that is, the formation of the first water ice layer which is in direct contact with interstellar silicates. Our simulations show that atomic O adsorption is very favourable due to the formation of a peroxo group on the silicate surface, and that this O adatom can readily be hydrogenated by two H atoms that previously landed and diffused on the surface.

Astronomical observations of the major band associated with solid water (namely the one at ∼3.0μ) show that the first layers of the water ice mantles covering the interstellar grains grow at the skin of the molecular clouds, where the visual extinction A$_v$ is about 1.6 mag (e.g. Whittet et al. 2001, 2013; Boogert et al. 2013). This implies that a water first layer is readily formed as soon as oxygen and hydrogen atoms are available in the gas. In this respect, our computations confirm on a theoretical basis the easy hydrogenation of the oxygen atoms on the bare silicates. On the other hand, astro-

chemical models (to the best of our knowledge) usually assume that the O hydrogenation into water molecules occurs on the bare silicate surfaces with the same energetic and rate constants than those used to model the O hydrogenation on the water ice surfaces. Specifically, the major difference between the two cases is the larger adsorption energy of oxygen atoms on the bare silicate (around 16000 K in our study) with respect to the water surface (between 800 and 2200 K; e.g. Wakelam et al. 2017). The larger adsorption energy of O atoms on the bare silicate surfaces assures a (much) larger residence time of these O atoms, which would easily saturate the chemisorption sites of the silicate grain. However, despite the incorrect values used in the astrochemical models, the impact on the predictions of iced water abundances is practically negligible, as the abundance is rather dominated by the growth on the water ices. On the other hand, this large reservoir of O atoms chemisorbed on the bare silicates may trigger/facilitate other reactions leading to trace low abundant species.

Importantly, our new computations shed light on, and likely solve, the long standing controversy caused by the disagreement between the measured and previously computed desorption energy of O atoms. As mentioned, Goumans et al. (2009a) computed a value of ($\approx$103 kcal mol^{-1}) whereas laboratory experiments by Vidali and coworkers (He, Jing & Vidali 2014; He et al. 2015) measured a value between 3.5 and 3.7 kcal mol^{-1} (namely 1764–1850 K). In order to understand where the discrepancy comes from, we recall here that, in the mentioned experiments, the O atoms were deposited on bare amorphous silicate films using a radio-frequency dissociated oxygen beam-line and the O desorption energies were obtained by means of temperature programmed desorption (TPD) measurements. In the experiments, therefore, due to their procedure, the first occurring surface event is the saturation of all the available O adsorption sites, so that the silicate films become fully oxygenated. According to our results, the O atoms involved in this first adsorption event are strongly chemisorbed so that the silicate films are in the form of O-rich silicate surfaces. Once all the silicate surface adsorption sites are fully occupied, the following incoming O atoms from the beam-line adsorb on the O-rich surface. Because of that, the atom/surface interactions are based on O$_{atom}$–O$_{surface}$ driven by dispersion forces so that the new O adatoms are physisorbed. According to this view, we here suggest that adsorption of O atoms on silicate surfaces takes place in two successive regimes: first, an O-chemisorbed layer is formed due to the direct interaction of O atoms with silicate adsorption sites; then, an O-physisorbed layer is formed due to the interaction of O atoms with the O-rich silicate. If this would be the case, the desorption energy values provided by Vidali and coworkers (He et al. 2014, 2015) are not for the chemisorbed O atoms but for the physisorbed ones. In other words, we predict that if the experiment were carried out (also) at larger temperatures, there would be a second peak of desorbed atoms.

Interestingly, similar explanations can be used to understand the different values of the binding energies of OH and H$_2$O calculated in this work (i.e. 13877 and 12261 K, respectively) and the desorption energies derived experimentally by Dulieu et al. (2013), Minissale et al. (2016) and Cazaux et al. (2016); i.e. 4600 and 4800 K, respectively. It is possible that these latter values are associated with the desorption of OH/H$_2$O molecules formed on water ice layers, which in turn were previously formed in the beginning of the experiments, since they were initiated with the deposition of O atoms on the substrates followed by hydrogenation to form OH and H$_2$O. The binding mechanism of these two species is different and expectedly their interaction energy more favorable on silicates than on water ice. The fact that authors reported the same desorption energies for

the two substrates employed (i.e. amorphous silicates and compact amorphous water ice) seems to indicate that the species were not actually adsorbed on a pristine, clean silicate surface, but probably on nascent water layers coating the silicate substrate.

Finally, our calculations also provide a set of energetic parameters. In addition to the O adsorption energy, the desorption energies of OH and H$_2$O are provided, as well as the energy barriers (and the associated transition frequencies) of the H-diffusion and the reactive processes leading to the formation of OH and H$_2$O. All of these are valuable data that can be introduced in databases and can be used in astrochemical models. In relation to the desorption energies of OH and H$_2$O, it is worth mentioning that they are actually high: 27.6 kcal mol^{-1} (13877 K) and 24.4 kcal mol^{-1} (12261 K), respectively. We conclude with perspective that similar computations considering the amorphous water surface as substrate are under way from us, so to complete the energetic and kinetic of the water ice mantle formation in the densest regions of the ISM.

7 CONCLUSIONS

In this work, formation of interstellar H$_2$O on the crystalline (010) Mg$_2$SiO$_4$ surface model, aiming to simulate the formation of the first water ice layer covering the silicate core of dust grains, has been investigated in detail by means of a quantum mechanical approach based on periodic density functional calculations. The reaction of water formation studied is the hydrogenation of atomic oxygen; that is, H + O → OH and H + OH → H$_2$O adopting a Langmuir–Hinshelwood mechanism. The processes of adsorption, diffusion, and chemical reaction involved in the overall reaction have been studied using the B3LYP-D2* method combined with flexible polarized Gaussian-type basis sets, which allows a balanced description of the species/surface interactions for both minima and activated complexes. The most interesting points emerging from this work are as follows.

Adsorption of atomic O on the (010) Mg$_2$SiO$_4$ surface model leads to the formation of a peroxo 'O$_2^{2-}$' group, in which the O adatom binds with an O atom of the surface, with a zero point energy (ZPE) corrected adsorption energy of -33.6 kcal mol^{-1}. Formation of this peroxo group is due to a charge transfer from the surface O atom to the adsorbing O atom. This adsorption event occurs in the singlet electronic state. As the ground electronic state of atomic oxygen is ^{3}P, a triplet → singlet spin crossing has been elucidated to take place during the adsorption process at a O$_{atom}$–surface distance of about 2.3 Å. The very favorable O adsorption energy points out interstellar silicates can efficiently trap O atoms for a very long time becoming good reservoirs of these species in the ISM, an aspect of fundamental relevance due to the low densities.

It is suggested that O adsorption on silicates can take place preferentially through chemisorption, due to the direct, strong interaction between O atoms and silicate adsorption sites. After all those sites are occupied, physisorption will take place, in which the incoming O atoms interact with the chemisorbed ones. According to this view, the experimental O desorption estimates ($\approx$ 3-4 kcal mol^{-1}) relate to physisorbed O atoms.

Formation of OH as central intermediate and H$_2$O as final product requires the adsorption and diffusion of two H atoms on the surface. Two possible H adsorption sites have been identified: one on the outermost Mg cations, leading to physisorption, and the other on surface O atoms, leading to chemisorption, with ZPE-corrected adsorption energies of about -4 to -5 and -68 to -83 kcal mol^{-1}, respectively. The H-diffusion from the physisorption to the chemisorption states takes place through low ZPE-corrected en-

ergy barriers (between 4–6 kcal mol^{-1}). These values contrast with the energy barriers associated with the formation of OH and H_2O (between 22–23 kcal mol^{-1}), in which the chemisorbed atoms react with the adsorbed O and OH species, respectively. The desorption energies for OH and H_2O have been computed to be 27.6 and 24.4 kcal mol^{-1}.

A kinetic analysis, including tunneling contributions adopting a semiclassical approach, indicate that the surface processes considered; namely, the H-diffusion and H reaction leading to OH and H_2O formation, are plausible reaction channels at the very low temperatures of the ISM if tunneling effects operate. Within this tunneling regime, H-diffusion is fast, while formation of OH and H_2O are the actual kinetic bottlenecks of the overall reaction, as the estimated rate constants are low.

The present work is the first one of a series of theoretical studies on water formation in the ISM on silicate surfaces, with the aim to provide an atomic-scale picture, including quantitative energetic data, of the current surface-mediated water formation network (Hama & Watanabe 2013). To this end, simulations on water formation by H addition to O_2 and O_3, and reaction of O with H_2 on silicates modeled by both extended surfaces (like the used one in this work) as well as finite nanosized cluster models (like the ones developed by Bromley and coworkers (Goumans & Bromley 2011; Kerkeni & Bromley 2013; Kerkeni et al. 2017)) are ongoing.

ACKNOWLEDGEMENTS

REFERENCES

Accolla M., Congiu E., Manicò G., Dulieu F., Chaabouni H., Lemaire J. L., Pirronello V., 2013, MNRAS, 429, 3200
Amari S., Anders E., Virag A., Zinner E., 1990, Nature, 345, 238
Asaduzzaman A. M., Laref S., Deymier P. A., Runge K., Cheng H.-P., Muralidharan K., Drake M. J., 2013, Phil. Trans. R. Soc. A, 371
Becke A. D., 1993, J. Chem. Phys., 98, 5648
Boogert A. C. A. et al., 2008, ApJ, 678, 985
Boogert A. C. A. et al., 2013, ApJ, 777, 73
Bowey J. E., Rawlings M. G., Adamson A. J., 2004, MNRAS, 348, L13
Caux E. et al., 1999, A&A, 347, L1
Cazaux S., Minissale M., Dulieu F., Hocuk S., 2016, A&A, 585, A55
Cazaux S., Tielens A. G. G. M., 2002, ApJ, 575, L29
Ceccarelli C., Caselli P., Bockelée-Morvan D., Mousis O., Pizzarello S., Robert F., Semenov D., 2014, in Beuther H., Klessen R. S., Dullemond C. P., Henning T., eds, Protostars and Planets VI. University of Arizona Press, Tucson, p. 914
Ceccarelli C., Hollenbach D. J., Tielens A. G. G. M., 1996, ApJ, 471, 400
Ceccarelli C. et al., 1999, A&A, 342, L21

Cernicharo J., Gonzalez-Alfonso E., Alcolea J., Bachiller R., John D., 1994, ApJ, 432, L59
Cernicharo J. et al., 1997, A&A, 323, L25
Chaabouni H. et al., 2012, J. Chem. Phys., 137, 234706
Civalleri B., D'Arco P., Orlando R., Saunders V. R., Dovesi R., 2001, Chem. Phys. Lett., 348, 131
Civalleri B., Maschio L., Ugliengo P., Zicovich-Wilson C. M., 2010, Phys. Chem. Chem. Phys., 12, 6382
Civalleri B., Zicovich-Wilson C. M., Valenzano L., Ugliengo P., 2008, CrystEngComm, 10, 405
Crimier N., Ceccarelli C., Lefloch B., Faure A., 2009, A&A, 506, 1229
Cuppen H. M., Ioppolo S., Romanzin C., Linnartz H., 2010, Phys. Chem. Chem. Phys., 12, 12077
de Leeuw N. H., Parker S. C., Catlow C. R. A., Price G. D., 2000, Phys. Chem. Minerals, 27, 332
De Looze I., Barlow M. J., Swinyard B. M., Rho J., Gomez H. L., Matsuura M., Wesson R., 2017, MNRAS, 465, 3309
Di Valentin C., Ferullo R., Binda R., Pacchioni G., 2006, Surf. Sci., 600, 1147
Doll K., 2001, Comput. Phys. Comm., 137, 74
Doty S. D., Neufeld D. A., 1997, ApJ, 489, 122
Dovesi R. et al., 2014, Int. J. Quantum Chem., 114, 1287
Downing C. A., Ahmady B., Catlow C. R. A., de Leeuw N. H., 2013, Phil. Trans. R. Soc. A, 371
Draine B. T., Li A., 2007, ApJ, 657, 810
Duley W. W., 1988, MNRAS, 234, 61P
Duley W. W., 1994, ApJ, 430, L133
Dulieu F., Amiaud L., Congiu E., Fillion J.-H., Matar E., Momeni A., Pirronello V., Lemaire J. L., 2010, A&A, 512, A30
Dulieu F., Congiu E., Noble J., Baouche S., Chaabouni H., Moudens A., Minissale M., Cazaux S., 2013, Sci. Rep., 3, 1338
Eckart C., 1930, Phys. Rev., 35, 1303
Eley D. D., 1941, Proc. R. Soc. London, 178, 452
Eley D. D., Rideal E. K., 1940, Nature, 146, 401
Fermann J. T., Auerbach S., 2000, J. Chem. Phys., 112, 6787
FIurton D. G., Laiho J. W., Witt A. N., 1999, ApJ, 526, 752
Fogerty S., Forrest W., Watson D. M., Sargent B. A., Koch I., 2016, Astrophys. J., 830, 71
Frisch M. J. et al., 2009, Wallingford CT.
Gamallo P., Sayos R., 2007, Phys. Chem. Chem. Phys., 9, 5112
Garcia-Gil S., Teillet-Billy D., Rougeau N., Sidis V., 2013, J. Phys. Chem. C, 117, 12612
Geneste G., Morillo J., Finocchi F., 2005, J. Chem. Phys., 122, 174707
Gibb E. L., Whittet D. C. B., Boogert A. C. A., Tielens A. G. G. M., 2004, ApJS, 151, 35
Gillett F. C., Forrest W. J., 1973, ApJ, 179, 483
Goumans T. P. M., Bromley S. T., 2011, MNRAS, 414, 1285
Goumans T. P. M., Catlow C. R. A., Brown W. A., Kästner J., Sherwood P., 2009a, Phys. Chem. Chem. Phys., 11, 5431
Goumans T. P. M., Richard C., Catlow A., Brown W. A., 2009b, MNRAS, 393, 1403
Grimme S., 2006, J. Comput. Chem., 27, 1787
Güdel M. et al., 2014, in Beuther H., Klessen R. S., Dullemond C. P., Henning T., eds, Protostars and Planets VI. University of Arizona Press, Tucsonp. 914
Hama T., Watanabe N., 2013, Chem. Rev., 113, 8783
Harris J., Kasemo B., 1981, Surf. Sci., 105, L281
He J., Jing D., Vidali G., 2014, Phys. Chem. Chem. Phys., 16, 3493
He J., Shi J., Hopkins T., Vidali G., Kaufman M. J., 2015, ApJ, 801, 120
Henning T., 2010, ARA&A, 48, 21
Herbst E., Klemperer W., 1973, ApJ, 185, 505
Herpin F. et al., 2017, A&A, 606, A52
Hinshelwood C. N., 1930, Annu. Res. London Chem. Soc., 27, 11
Hollenbach D., Kaufman M. J., Bergin E. A., Melnick G. J., 2009, ApJ, 690, 1497
Hollenbach D., McKee C. F., 1989, ApJ, 342, 306
Hoyle F., Wickramasinghe N. C., 1969, Nature, 223, 459

Ioppolo S., Cuppen H. M., Romanzin C., van Dishoeck E. F., Linnartz H., 2008, ApJ, 686, 1474

Ioppolo S., Cuppen H. M., Romanzin C., van Dishoeck E. F., Linnartz H., 2010, Phys. Chem. Chem. Phys., 12, 12065

Jiao H., Gianfranco V., 2014, ApJ, 788, 50

Jing D., He J., Bonini M., Brucato J. R., Vidali G., 2013, J. Phys. Chem. A, 117, 3009

Jing D., He J., Brucato J., Sio A. D., Tozzetti L., Vidali G., 2011, ApJ, 741, L9

Jones A. P., Fanciullo L., Köhler M., Verstraete L., Guillet V., Bocchio M., Ysard N., 2013, A&A, 558, A62

Kantorovich L. N., Gillan M. J., 1997, Surf. Sci., 374, 373

Karska A. et al., 2013, A&A, 552, A141

Katz N., Furman I., Biham O., Pirronello V., Vidali G., 1999, ApJ, 522, 305

Kerkeni B., Bacchus-Montabonel M.-C., Bromley S. T., 2017, Mol. Astrophys., 7, 1

Kerkeni B., Bromley S. T., 2013, MNRAS, 435, 1486

King H. E., Stimpfl M., Deymier P., Drake M. J., Catlow C. R. A., Putnis A., de Leeuw N. H., 2010, Earth Planet. Sci. Lett., 300, 11

Kristensen L. E. et al., 2012, A&A, 542, A8

Lamberts T., Cuppen H. M., Fedoseev G., Ioppolo S., Chuang K.-J., Linnartz H., 2014, A&A, 570, A57

Lamberts T., Samanta P. K., Köhn A., Kästner J., 2016, Phys. Chem. Chem. Phys., 18, 33021

Langmuir I., 1922, Trans. Faraday Soc., 17, 621

Lee C., Yang W., Parr R. G., 1988, Phys. Rev. B, 37, 785

Leeuw N. H. d., Catlow C. R. A., King H. E., Putnis A., Muralidharan K., Deymier P., Stimpfl M., Drake M. J., 2010, Chem. Commun., 46, 8923

Li A., Draine B. T., 2001, ApJ, 550, L213

Li M. P., Zhao G., Li A., 2007, MNRAS, 382, L26

Lis D. C., Jocelyn K., Phillips T. G., Schilke P., Werner M. W., Zmuidzinas J., 2001, ApJ, 561, 823

Liseau R. et al., 1996, A&A, 315, L181

Liu L. et al., 2017, ApJ, 846, 5

Matar E., Congiu E., Dulieu F., Momeni A., Lemaire J. L., 2008, A&A, 492, L17

Meisner J., Lamberts T., Kästner J., 2017, ACS Earth Space Chem., 1, 399

Minissale M., Dulieu F., Cazaux S., Hocuk S., 2016, A&A, 585, A24

Miyauchi N., Hidaka H., Chigai T., Nagaoka A., Watanabe N., Kouchi A., 2008, Chem. Phys. Lett., 456, 27

Mokrane H., Chaabouni H., Accolla M., Congiu E., Dulieu F., Chehrouri M., Lemaire J. L., 2009, ApJ, 705, L195

Monkhorst H. J., Pack J. D., 1976, Phys. Rev. B, 13, 5188

Morisset S., Aguillon F., Sizun M., Sidis V., 2003, Phys. Chem. Chem. Phys., 5, 506

Muralidharan K., Deymier P., Stimpfl M., de Leeuw N. H., Drake M. J., 2008, Icarus, 198, 400

Navarro-Ruiz J., Martínez-González J. A., Sodupe M., Ugliengo P., Rimola A., 2015, MNRAS, 453, 914

Navarro-Ruiz J., Sodupe M., Ugliengo P., Rimola A., 2014a, Phys. Chem. Chem. Phys., 16, 17447

Navarro-Ruiz J., Ugliengo P., Rimola A., Sodupe M., 2014b, J. Phys. Chem. A, 118, 5866

Navarro-Ruiz J., Ugliengo P., Sodupe M., Rimola A., 2016, Chem. Commun., 52, 6873

Oba Y., Miyauchi N., Hidaka H., Chigai T., Watanabe N., Kouchi A., 2009, ApJ, 701, 464

Oba Y., Osaka K., Watanabe N., Chigai T., Kouchi A., 2014, Faraday Discuss., 168, 185

Oba Y., Watanabe N., Hama T., Kuwahata K., Hidaka H., Kouchi A., 2012, ApJ, 749, 67

Oba Y., Watanabe N., Kouchi A., Hama T., Pirronello V., 2011, Phys. Chem. Chem. Phys., 13, 15792

Omont A. et al., 2011, A&A, 530, L3

Omont A. et al., 2013, A&A, 551, A115

Pascale F., Zicovich-Wilson C. M., Gejo F. L., Civalleri B., Orlando R., Dovesi R., 2004, J. Comput. Chem., 25, 888

Pasti I. A., Baljozovic M., Skorodumova N. V., 2015, Surf. Sci., 632, 39

Pirronello V., Biham O., Liu C., Shen L., Vidali G., 1997b, ApJ, 483, L131

Pirronello V., Liu C., Shen L., Vidali G., 1997a, ApJ, 475, L69

Prigiobbe V., Suarez Negreira A., Wilcox J., 2013, J. Phys. Chem. C, 117, 21203

Rimola A., Civalleri B., Ugliengo P., 2010a, Phys. Chem. Chem. Phys., 12, 6357

Rimola A., Trigo-Rodriguez J. M., Martins Z., 2017, Phys. Chem. Chem. Phys., 19, 18217

Rimola A., Zicovich-Wilson C. M., Dovesi R., Ugliengo P., 2010b, J. Chem. Theory Comput., 6, 1341

Romanzin C., Ioppolo S., Cuppen H. M., Dishoeck E. F.v., Linnartz H., 2011, J. Chem. Phys., 134, 084504

Schafer A., Horn H., Ahlrichs R., 1992, J. Chem. Phys., 97, 2571

Silva L., Vladilo G., Murante G., Provenzale A., 2017, MNRAS, 470, 2270

Taquet V., Peters P. S., Kahane C., Ceccarelli C., López-Sepulcre A., Toubin C., Duflot D., Wiesenfeld L., 2013, A&A, 550, A127

Tielens A. G. G. M., Hagen W., 1982, A&A, 114, 245

van Dishoeck E. F., Herbst E., Neufeld D. A., 2013, Chem. Rev., 113, 9043

van Dishoeck E. F. et al., 2011, PASP, 123, 138

Vidali G., 2013, Chem. Rev., 113, 8762

Vidali G., Li L., Roser J. E., Badman R., 2009, Adv. Space Res., 43, 1291

Wakelam V. et al., 2017, Mol. Astrophys., 9, 1

Whittet D. C. B., Bode M. F., Longmore A. J., Adamson A. J., McFadzean A. D., Aitken D. K., Roche P. F., 1988, MNRAS, 233, 321

Whittet D. C. B., Gerakines P. A., Hough J. H., Shenoy S. S., 2001, ApJ, 547, 872

Whittet D. C. B., Poteet C. A., Chiar J. E., Pagani L., Bajaj V. M., Horne D., Shenoy S. S., Adamson A. J., 2013, ApJ, 774, 102

Witt A. N., Gordon K. D., Furton D. G., 1998, ApJ, 501, L111

Witt A. N., Schild R. E., 1988, ApJ, 325, 837

Woon D. E., Dunning T. H., Jr, 1994, J. Chem. Phys., 100, 2975

Yu X., Zhang X., Tian X., Wang S., Feng G., 2015, Appl. Surf. Sci., 324, 53

Zolensky M. E. et al., 2006, Science, 314, 1735

SUPPORTING INFORMATION

Supplementary data are available at *MNRAS* online.

APPENDIX: ON-LINE MATERIAL.

Please note: Oxford University Press is not responsible for the content or functionality of any supporting materials supplied by the authors. Any queries (other than missing material) should be directed to the corresponding author for the article.

APPENDIX: ON-LINE MATERIAL

In the on-line material file we provide: (i) the results for the calibration study for the O adsorption on a minimal cluster model of forsterite, (ii) the Mulliken charges and spin densities of different optimized systems, (iii) optimization snapshots when a H atom is adsorbed on the O_{Fo3} atom, and (iv) calculated desorption energy curves for OH and H_2O from the Fo–OH and Fo–H_2O systems.

This paper has been typeset from a TEX/LATEX file prepared by the author.